International Journal of Solids and Structures xxx (xxxx) 114121

Contents lists available at ScienceDirect

International Journal of Solids and Structures

journal homepage: www.elsevier.com/locate/ijsolstr

Pin–hole contact with curvature-induced couple tractions in couple-stress elasticity

E. Radi [a, b, *], M. A. Güler [c]

[a] DISMI – Dipartimento di Scienze e Metodi dell'Ingegneria, Università di Modena e Reggio Emilia, Via G. Amendola 2, I-42122 Reggio Emilia, Italy
[b] En&Tech – Centro di Ricerca Interdipartimentale per la Ricerca Industriale ed il Trasferimento Tecnologico, Piazzale Europa, 1, 42122 Reggio Emilia, Italy
[c] College of Engineering and Technology, American University of the Middle East, Egaila 54200, Kuwait

ARTICLE INFO

Keywords:
Pin-hole contact
Curvature compatibility
Transmitted couple tractions
Constrained couple-stress elasticity
Coupled dual series equations

ABSTRACT

In this study, a curvature-compatible formulation is presented for the frictionless contact between a rigid pin and a circular hole in a microstructured elastic plane governed by constrained couple-stress theory under plane-strain conditions. Unlike the classical micro-free assumption, the present model allows transmission of couple tractions across the contact interface and imposes a uniform tangential curvature, consistent with the pin-hole geometry. The boundary value problem is expressed through trigonometric expansions in polar coordinates, yielding a coupled system of dual series equations that is reduced to an infinite algebraic system and solved by truncation. The effect of transmitted couple tractions on the contact half-angle and on the stress and couple-stress fields along the hole boundary is quantified. The results show that curvature compatibility significantly modifies the near-boundary response and leads to a more uniform stress and couple-stress distribution compared with the micro-free case. The formulation provides a consistent extension of pin-hole contact analysis in materials with intrinsic length-scale effects.

1. Introduction

Contact mechanics of micro- and nano-structured materials exhibit size-dependent behavior under highly localized deformations, such as those arising in pin-loaded hole configurations. Such configurations are commonly encountered in micro-scale applications including micro-electro-mechanical systems (MEMS) and nano-electro-mechanical systems (NEMS) joints and pivots, micro-gripper mechanisms, compliant hinges, micro-shaft and micro-bearing interfaces, and precision positioning and micro/nano-positioning devices. For example, Zhang et al. (2007) proposed a flexure-based pivot structure for external-cavity MEMS tunable lasers in which load-dependent contact occurs between conjugate curved surfaces. Similarly, Verotti et al. (2015) introduced a MEMS-based conjugate-surfaces flexure hinge combining a curved beam with a pair of contacting profiles whose interaction depends on the applied load. Related compliant MEMS systems have also been developed for piezoelectric-driven microgrippers (Wang et al., 2011), cell-manipulation microgrippers (Belfiore et al., 2013), and micro- and nanopositioning stages (Bashash and Jalili, 2009; Polit and Dong, 2011; Xu, 2012). Beyond the microscale, analogous flexural pivot concepts have been investigated in precision mechatronic systems, where localized stress and load transfer near hinge-like regions govern performance and fatigue behavior (Peterson et al., 2023). In order to reliably predict load transfer, stress localization, wear, and failure in such systems, the contact model must be capable of incorporating intrinsic material length-scale effects associated with microstructural interactions near the contact zone.

Generalized continuum theories provide a natural framework for capturing these effects without resorting to atomistic simulations. Among them, couple-stress elasticity (also referred to as Cosserat elasticity with constrained rotations) incorporates intrinsic material length scales by accounting for resistance to curvature and rotation gradients, which become pronounced in localized deformation fields typical of contact problems. The theoretical foundations of such models were established in the seminal works of Eringen and co-workers and later applied to stress concentration and hole problems by Mindlin (1963), Weitsman (1965), Hartranft and Shih (1965), and Ariman (1967). Subsequent studies, including Das (1969), demonstrated that couple-stresses can substantially modify stress distributions near pin–hole interfaces, highlighting the importance of micro-rotational effects even though a fully consistent contact formulation was not addressed.

* E-mail address: eradi@unimore.it (E. Radi)
E-mail addresses: eradi@unimore.it (E. Radi), mehmet.guler@aum.edu.kw (M.A. Güler).

https://doi.org/10.1016/j.ijsolstr.2026.114121
Received 23 February 2026; Received in revised form 19 May 2026; Accepted 24 May 2026
0020-7683/

More broadly, extensive experimental and theoretical work on indentation and small-scale contact has shown that intrinsic length scales govern mechanical response when contact dimensions approach microstructural sizes. In metals, such size effects have been linked to geometrically necessary dislocations (Nix and Gao, 1998), while in polymers and other microstructured materials they have been attributed to curvature-dominated deformation, surface effects, and material inhomogeneity. These observations have been successfully interpreted using gradient and couple-stress theories in a variety of contact settings (e.g., Chong and Lam, 1999; Lam et al., 2003; Zisis et al., 2014; Gourgiotis et al., 2019), establishing a continuum basis for size-dependent contact mechanics.

The analytical solution to the frictionless contact problem of a rigid pin inserted into a hole with clearance in a couple-stress elastic medium was recently developed by the present authors (Radi and Güler, 2026). In that work, the contact interface was modeled as a micro-free boundary, characterized by zero couple tractions and arbitrary curvature. The results revealed pronounced size effects and a strongly load-dependent response of the contact pressure and radial displacement, providing new insight into pin-hole contact behavior at the microscale.

Although the micro-free contact condition is suitable for idealized smooth interfaces, it does not fully capture many practical micro-scale contact scenarios. In curved rigid–elastic contacts, the interface geometry itself imposes a kinematic constraint through curvature mismatch between the contacting bodies. For a rigid cylindrical pin engaging a circular hole, the tangential curvature along the contact arc can be assumed as uniform, though depending on the geometry and material parameters. Under these conditions, the mechanical response is influenced not only by tractions and couple tractions, but also by the induced curvature constraint, which activates additional microstructural mechanisms that are absent under micro-free contact assumptions.

In couple-stress elasticity, the microrotation characterizes the local orientation of microstructural entities such as grain lattices, inclusions, fibers, pores, micro-voids, or particles. Within the constrained couple-stress theory of elasticity developed by Koiter (1964) and adopted here, the microrotation field is not an independent kinematic variable but is constrained to coincide with the macroscopic rotation derived from the displacement field. Accordingly, the microrotation is identified with the skew-symmetric part of the displacement gradient. When a material element on the hole surface engage the rigid pin, its tangential curvature is modified according to the pin clearance and material characteristic length. This contact condition reflects the physical situation in which the rigid pin constrains the contacted material at the microscale, thereby inducing distributed couple tractions along the contact interface.

Motivated by these considerations, the present work extends the analytical solution of Radi and Güler (2026) for a rigid pin in advancing contact with the rim of a circular hole with small clearance in an infinite couple-stress elastic plane. The extension concerns the modeling of the contact interface. While the previous study assumed a micro-free interface with vanishing couple tractions, the present formulation prescribes a uniform tangential curvature along the contact region, thereby allowing couple-stress tractions to be transmitted across the interface. Outside the contact zone, both traction-free and couple-traction-free boundary conditions are retained.

Although the geometry, governing couple-stress framework, polar-series representation, and general solution strategy remain similar to those of the earlier work, the modified contact condition leads to a mechanically distinct response. In particular, the imposed curvature generates a distribution of couple tractions along the contact arc, in contrast to the classical couple-traction-free assumption and thereby providing a different micromechanical description of the contact interaction. This extension constitutes the main original contribution of the present study.

The solution is formulated in polar coordinates within the framework of constrained couple-stress elasticity, employing the general representations developed by Das (1969) and Bhandakkar (2023) to describe the associated mechanical fields in polar coordinates. Enforcing the classical condition on radial displacement (Persson, 1964) together with the assumption of a uniform tangential curvature along the contact arc leads to a set of coupled dual series equations. By generalizing the methodology proposed by Block and Keer, 2007 and previously applied by Radi and Strozzi (2023) and Radi and Güler (2026) for a single dual-series system, a novel procedure is developed here to reduce the problem to a coupled infinite linear system of algebraic equations for the unknown series coefficients. After series truncation, analytical expressions are obtained for the contact half-angle as well as the stress, couple-stress, displacement, and rotation fields over a range of loading levels and characteristic length scales.

This extended formulation enables a direct comparison between couple-traction-free and curvature-prescribed contact conditions, highlighting how curvature constraints affect contact pressure, radial displacement, stress concentration, and couple-stress distributions. While the overall qualitative trends remain similar, noticeable differences arise in the magnitude and spatial distribution of the mechanical fields, particularly at moderate-to-high loads where curvature and rotation gradients are significant. These results underscore the importance of incorporating microstructural curvature effects in the mechanics of cylindrical joints and pin-hole assemblies and provide new insights into size-dependent behavior in couple-stress elastic continua.

It is worth noting that the present formulation is restricted to the elastic regime and does not account for plastic deformation or dislocation activity. In ductile metallic systems at small scales, size-dependent plasticity may dominate the response once yielding occurs, as described by strain-gradient plasticity and discrete dislocation models (Gao et al., 2015). In contrast, the adopted couple-stress elasticity framework captures size effects associated with rotation gradients and microstructural bending stiffness in the pre-yield regime, and is therefore complementary to plasticity-based approaches. The present formulation is also restricted to frictionless contact in order to isolate the effect of higher-order elastic contributions associated with couple tractions. While friction may introduce additional corrections to the classical solution (Lee et al., 2018), the size-dependent effects captured by couple-stress elasticity can be significantly larger when the intrinsic material length scale is not negligible. Moreover, the inclusion of friction would introduce additional tangential tractions and coupling mechanisms at the interface, and would generally require a more complex formulation, likely involving numerical methods. Such an extension is beyond the scope of the present analytical study, but represents an interesting direction for future work.

2. Problem formulation

The problem concerns the frictionless interaction between a rigid cylindrical pin and a circular hole separated by a small radial clearance, $\delta \ll R$, within an unbounded medium governed by constrained couple-stress elasticity (Fig. 1). The material response is characterized by the shear modulus μ, Poisson's ratio ν, and the intrinsic length parameter ℓ. The hole radius is denoted by R, while the applied load P produces contact over an unknown angular region determined by the half-angle α, which increases with the load due to the presence of clearance.

A cylindrical coordinate system (r, θ) centered at the hole is employed, with $\theta = 0$ aligned with the direction of the applied force. Under plane-strain conditions, the field equations of couple-stress elasticity are expressed in terms of the two Mindlin–Airy stress functions. These functions satisfy the same governing relations and compatibility conditions adopted in Radi and Güler (2026), and are consistent with the classical formulations reported by Das (1969) and Bhandakkar (2023). In particular, the complete representation of the general solu-

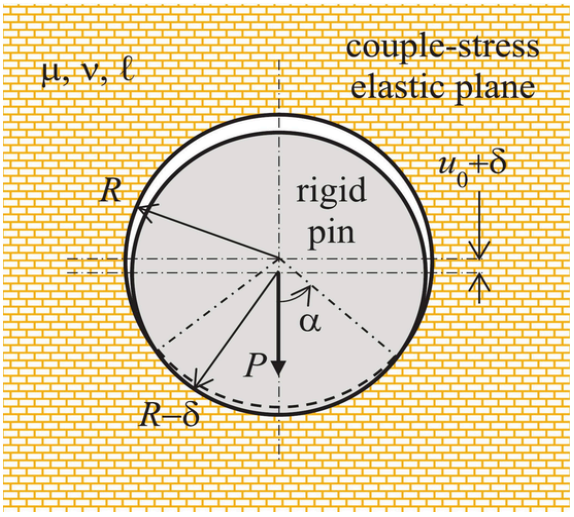

Fig. 1. Pin-hole contact configuration with clearance in a constrained couple-stress elastic medium.

tion in polar coordinates under the plane strain conditions for couple-stress elastic materials with constrained rotation was provided by Bhandakkar (2023). Here, an infinite plane is considered and, therefore, only the admissible terms of the Bhandakkar (2023) solutions which decay as r goes to infinity and yield single-valued displacements were retained. Then, the following stress, couple-stress, displacement, and microrotation components are assumed:

$$
\begin{aligned}
\frac{R\sigma_{rr}}{2\mu\delta} &= \frac{a_0}{\rho^2} + \left[\frac{b_1}{2}\left(\frac{3-2\nu}{1-\nu} - \frac{8\lambda^2}{\rho^2}\right) - \frac{2c_1}{\rho^2} + \frac{a_1}{\lambda}K_2\left(\frac{\rho}{\lambda}\right)\right]\frac{\cos\theta}{\rho} \\
&- \sum_{n=2}^{\infty}\left\{c_n\,\frac{n\,(n+1)}{\rho^{n+2}} + b_n\,(n-1)\left[\frac{n+2}{\rho^n} - 8\lambda^2(1-\nu)\,n\frac{n+1}{\rho^{n+2}}\right]\right. \\
&\left. - \frac{a_n}{2\lambda\rho}\left[(n-1)\,K_{n-1}\left(\frac{\rho}{\lambda}\right) + (n+1)\,K_{n+1}\left(\frac{\rho}{\lambda}\right)\right]\right\}\cos n\theta, \\
\frac{R\sigma_{\theta\theta}}{2\mu\delta} &= -\frac{a_0}{\rho^2} - \left[\frac{a_1}{\lambda}K_0\left(\frac{\rho}{\lambda}\right) + \frac{b_1}{2}\frac{1-2\nu}{1-\nu} - \frac{2c_1}{\rho^2}\right]\frac{\cos\theta}{\rho} \\
&+ \sum_{n=2}^{\infty}\left\{c_n n\,\frac{n+1}{\rho^{n+2}} + b_n\,(n-1)\left[\frac{n-2}{\rho^n} - 8\lambda^2(1-\nu)\,n\frac{n-1}{\rho^{n+2}}\right]\right. \\
&\left. - \frac{a_n}{2\lambda\rho}\left[(n+1)\,K_{n-1}\left(\frac{\rho}{\lambda}\right) + (n-1)\,K_{n+1}\left(\frac{\rho}{\lambda}\right)\right]\right\}\cos n\theta, \\
\frac{R\sigma_{r\theta}}{2\mu\delta} &= \left[\frac{a_1}{\lambda}K_2\left(\frac{\rho}{\lambda}\right) - \frac{b_1}{2}\left(\frac{1-2\nu}{1-\nu} + \frac{8\lambda^2}{\rho^2}\right) - \frac{2c_1}{\rho^2}\right]\frac{\sin\theta}{\rho} \\
&- \sum_{n=2}^{\infty}\left\{c_n n\frac{n+1}{\rho^{n+2}} + b_n n\frac{n-1}{\rho^n}\left[1 - 8\lambda^2(1-\nu)\frac{n+1}{\rho^2}\right]\right. \\
&\left. - \frac{a_n}{2\lambda\rho}\left[(n+1)\,K_{n+1}\left(\frac{\rho}{\lambda}\right) - (n-1)\,K_{n-1}\left(\frac{\rho}{\lambda}\right)\right]\right\}\sin n\theta, \\
\frac{R\sigma_{\theta r}}{2\mu\delta} &= \left\{\frac{a_1}{\lambda}\left[\frac{\rho}{\lambda}K_1\left(\frac{\rho}{\lambda}\right) + K_2\left(\frac{\rho}{\lambda}\right)\right] - \frac{b_1}{2}\left(\frac{1-2\nu}{1-\nu} + \frac{8\lambda^2}{\rho^2}\right) - \frac{2c_1}{\rho^2}\right\}\frac{\sin\theta}{\rho} \\
&- \sum_{n=2}^{\infty}\left\{c_n n\frac{n+1}{\rho^{n+2}} + b_n n\,(n-1)\left[\frac{1}{\rho^n} - 8\lambda^2(1-\nu)\,\frac{n+1}{\rho^{n+2}}\right]\right. \\
&\left. - \frac{a_n}{\lambda}\left[K_{n-1}\left(\frac{\rho}{\lambda}\right) + \left(\frac{1}{\lambda} + n\,(n+1)\,\rho^2\lambda\right)K_n\left(\frac{\rho}{\lambda}\right)\right]\right\}\sin n\theta, \\
\frac{m_r}{2\mu\delta} &= \left\{2b_1\frac{\lambda^2}{\rho^2} - \frac{a_1}{2\lambda}\left[K_0\left(\frac{\rho}{\lambda}\right) + K_2\left(\frac{\rho}{\lambda}\right)\right]\right\}\sin\theta \\
&- \sum_{n=2}^{\infty}\left\{b_n\,8\lambda^2(1-\nu)\,n\frac{n-1}{\rho^{n+1}} + \frac{a_n}{2\lambda}\left[K_{n-1}\left(\frac{\rho}{\lambda}\right) + K_{n+1}\left(\frac{\rho}{\lambda}\right)\right]\right\}\sin n\theta, \\
\frac{m_\theta}{2\mu\delta} &= \left[\frac{a_1}{\rho}K_1\left(\frac{\rho}{\lambda}\right) - 2b_1\frac{\lambda^2}{\rho^2}\right]\cos\theta \\
&+ \sum_{n=2}^{\infty}\left[8b_n\,\lambda^2(1-\nu)\,\frac{n-1}{\rho^{n+1}} + \frac{a_n}{\rho}K_n\left(\frac{\rho}{\lambda}\right)\right]n\,\cos n\theta,
\end{aligned}
\tag{2.1}
$$

$$
\begin{aligned}
\frac{u_r}{\delta} &= -\frac{a_0}{\rho} + \left\{b_1\left[\frac{2\lambda^2}{\rho^2} - \frac{1-(3-4\nu)\ln\rho}{2(1-\nu)}\right] + \frac{c_1}{\rho^2} - \frac{a_1}{\rho}K_1\left(\frac{\rho}{\lambda}\right)\right\}\cos\theta \\
&+ \sum_{n=2}^{\infty}\left\{\frac{n\,c_n}{\rho^{n+1}} + \left[\frac{n+2-4\nu}{\rho^{n-1}} - 8\lambda^2(1-\nu)\,n\frac{n-1}{\rho^{n+1}}\right]b_n - \frac{a_n}{\rho}nK_n\left(\frac{\rho}{\lambda}\right)\right\}\cos n\theta, \\
\frac{u_\theta}{\delta} &= \left\{b_1\left[\frac{2\lambda^2}{\rho^2} - \frac{3-4\nu}{2(1-\nu)}\ln\rho\right] + \frac{c_1}{\rho^2} - \frac{a_1}{2\lambda}\left[K_0\left(\frac{\rho}{\lambda}\right) + K_2\left(\frac{\rho}{\lambda}\right)\right]\right\}\sin\theta \\
&+ \sum_{n=2}^{\infty}\left\{\frac{n\,c_n}{\rho^{n+1}} + \left[\frac{n-4+4\nu}{\rho^{n-1}} - 8\lambda^2(1-\nu)\,n\frac{n-1}{\rho^{n+1}}\right]b_n\right. \\
&\left. - \frac{a_n}{2\lambda}\left[K_{n-1}\left(\frac{\rho}{\lambda}\right) + K_{n+1}\left(\frac{\rho}{\lambda}\right)\right]\right\}\sin n\theta, \\
\frac{R\omega_z}{\delta} &= \left[\frac{a_1}{2\lambda^2}K_1\left(\frac{\rho}{\lambda}\right) - \frac{b_1}{\rho}\right]\sin\theta \\
&+ \sum_{n=2}^{\infty}\left[4(1-\nu)\,\frac{n-1}{\rho^n}b_n + \frac{a_n}{2\lambda^2}K_n\left(\frac{\rho}{\lambda}\right)\right]\sin n\theta,
\end{aligned}
$$

where $\rho = r/R$, $\lambda = \ell/R$, K_n is the Bessel function of the second kind of order n, which satisfy the following recursive relation:

$$
K_{n-1}(z) + \frac{2n}{z}K_n(z) - K_{n+1}(z) = 0 \tag{2.2}
$$

and the unknown constants a_0, and a_n, b_n, c_n, for $n = 1,2,3, \ldots$, can be calculated by imposing the frictionless contact conditions between the rigid pin and the hole rim, at $\rho = 1$, by taking into account also the couple tractions.

The key distinction of the present study lies in the contact boundary conditions. In the earlier work (Radi and Güler, 2026), the contact interface was modeled as micro-free, with zero couple tractions and prescribed radial displacement along the contact arc. In the present formulation, instead of vanishing of the couple tractions, a new boundary condition is assumed on the curvature along the contact arc, which follows from the contact condition with the rigid pin, while traction-free and couple-traction-free conditions remain enforced outside the contact zone.

The variation of the geometrical curvature κ_g of the elements on the hole rim in contact with the rigid pin is given by the difference between the pin curvature $1/(R-\delta)$ and the hole curvature $1/R$, namely $\kappa_g = \delta/R^2$, for $\delta \ll R$. This curvature would be the ideal curvature if the deformation perfectly followed the rigid geometry of the pin. However, in a couple-stress material, the curvature along the contact zone is influenced by both the geometrical curvature and the material resistance to rotational deformation. The material resists changes in the rotational field (i.e., it resists the bending that causes curvature), and this resistance depends on the material characteristic length ℓ, which characterizes the material ability to resist gradients of rotation. The total curvature κ_0 at any point along the contact arc is therefore the sum of the geometrical curvature and a material-dependent contribution that smooths the curvature depending on ℓ. When ℓ is large compared to the contact zone the curvature is significantly smoothed out by the material resistance to bending. Therefore, along the contact arc, $0 \le |\theta| \le \alpha$, the rigid pin kinematics allows to prescribe contact conditions both on the radial displacement and the curvature. The former condition is the same as that considered in the work of Radi and Güler (2026), while the latter assume a uniform curvature κ_0 of the material elements lying on the hole surface in contact with the rigid pin, where κ_0 is unknown. Since the tangential curvature is $\kappa_{\theta z} = \omega_{z,\theta}/R$, it follows $\omega_{z,\theta} = R\kappa_0$ along the contact arc. Therefore, the set of contact conditions at $\rho = 1$ considered here is

$$
\begin{aligned}
\sigma_{r\theta} &= 0, \quad \text{for } 0 \leqslant |\theta| \leqslant \pi, \\
\sigma_{rr} &= 0, \quad m_r = 0, \quad \text{for } \alpha \leqslant |\theta| \leqslant \pi, \\
u_r &= u_0\,\cos\theta - \delta\,(1-\cos\theta), \quad \omega_{z,\theta} = \kappa_0 R, \quad \text{for } 0 \leqslant |\theta| \leqslant \alpha,
\end{aligned}
\tag{2.3}
$$

where α and u_0 denote the contact half-angle and the rigid body motion of the pin, respectively. Note that u_0 coincides with the radial displace-

ment of the hole rim at $\theta = 0$, namely $u_r(1, 0) = u_0$. The contact condition on the radial displacement holds for a cylindrical pin in a hole with small clearance $\delta \ll R$. It was introduced by Persson (1964) and recently used by Radi and Güler (2026).

The assumption of a uniform curvature condition over the contact region, allows the transmission of couple-stress tractions at the interface, thus leading to a different micromechanical description of the contact interaction, and it constitutes the main novelty introduced by the present work.

The geometric mismatch between the rigid pin and the hole provides a characteristic curvature scale, $\kappa_g = \delta/R^2$, but does not by itself determine the curvature field in the couple-stress medium, since the curvature tensor is a material quantity associated with rotation gradients and must satisfy the equilibrium equations together with the constitutive relations. The assumption of a uniform curvature along the contact arc is introduced here as a modeling idealization, corresponding to a rotationally constrained interface capable of transmitting couple tractions. Under this assumption, the microstructure in the boundary layer is prevented from developing relative spin variations along the contact interface, leading to a constant curvature measure. It is emphasized that the interfacial curvature κ_0 does not necessarily coincide with the geometric mismatch κ_g, as it also depends on the mechanical response of the material and the tangential displacement along the interface.

3. Reduction of the contact conditions to a system of coupled dual series equations

By introducing the fields (2.1) in the contact conditions $(2.3)_1$, the following relations are obtained for the constants c_1 and c_n that enter Eqs. (2.1):

$$c_1 = \frac{a_1}{2\lambda}K_2\left(\frac{1}{\lambda}\right) - \frac{b_1}{4}\left(8\lambda^2 + \frac{1-2\nu}{1-\nu}\right), \tag{3.1}$$

and

$$\begin{aligned} c_n = {} & b_n(n-1)\left[8\lambda^2(1-\nu) - \frac{1}{n+1}\right] \\ & + \frac{a_n}{2\lambda n}\left[K_{n+1}\left(\frac{1}{\lambda}\right) - \frac{n-1}{n+1}K_{n-1}\left(\frac{1}{\lambda}\right)\right], \end{aligned} \tag{3.2}$$

for $n \geq 2$. Then, the stress tractions, couple tractions, radial displacement and derivative of rotation, which enter the contact conditions (2.3) along the hole rim at $\rho = 1$, are

$$\begin{aligned} \frac{R\sigma_{rr}}{2\mu\delta} &= a_0 + 2b_1\cos\theta + \sum_{n=2}^{\infty}\left[\frac{a_n}{\lambda}K_{n-1}\left(\frac{1}{\lambda}\right) - 2b_n\right](n-1)\cos n\theta, \\ \frac{m_r}{2\mu\delta} &= \left\{2\lambda^2 b_1 - \frac{a_1}{2\lambda}\left[K_0\left(\frac{1}{\lambda}\right) + K_2\left(\frac{1}{\lambda}\right)\right]\right\}\sin\theta \\ &\quad - \sum_{n=2}^{\infty}\left\{\frac{a_n}{2\lambda}\left[K_{n-1}\left(\frac{1}{\lambda}\right) + K_{n+1}\left(\frac{1}{\lambda}\right)\right] + 8\lambda^2(1-\nu)(n-1)\,nb_n\right\}\sin n\theta, \\ \frac{u_r}{\delta} &= -a_0 + \left[\frac{a_1}{2\lambda}K_0\left(\frac{1}{\lambda}\right) - \frac{3-2\nu}{4(1-\nu)}b_1\right]\cos\theta \\ &\quad + \sum_{n=2}^{\infty}\left\{\frac{a_n}{\lambda}K_{n-1}\left(\frac{1}{\lambda}\right) + [4(1-\nu)(n+1) - 2]\,b_n\right\}\frac{\cos n\theta}{n+1}, \\ \frac{R\omega_{z,\theta}}{\delta} &= \left[\frac{a_1}{2\lambda^2}K_1\left(\frac{1}{\lambda}\right) - b_1\right]\cos\theta \\ &\quad + \sum_{n=2}^{\infty}\left[\frac{a_n}{2\lambda^2}K_n\left(\frac{1}{\lambda}\right) + 4(1-\nu)(n-1)\,b_n\right]n\,\cos n\theta. \end{aligned} \tag{3.3}$$

The contact conditions $(2.3)_{2,3}$ then write

$$\begin{aligned} &\frac{A_0}{2} + \sum_{n=1}^{\infty}A_n\cos n\theta = 0, \\ &\sum_{n=1}^{\infty}B_n\sin n\theta = 0, \end{aligned} \tag{3.4}$$

for $\alpha \leq |\theta| \leq \pi$, where

$$A_0 = 2a_0, A_1 = 2b_1, B_1 = [K_0(1/\lambda) + K_2(1/\lambda)]\,a_1 - 4\lambda^3 b_1, \tag{3.5}$$

$$A_n = (n-1)\left[\frac{a_n}{\lambda}K_{n-1}\left(\frac{1}{\lambda}\right) - 2b_n\right],$$

$$B_n = \left[K_{n-1}(1/\lambda) + K_{n+1}(1/\lambda)\right]\,a_n + 16\,\lambda^3(1-\nu)(n-1)\,nb_n, \text{for} \quad n \geq 2. \tag{3.6}$$

Moreover, using Eqs. (3.3), (3.5), and (3.6), the contact conditions $(2.3)_{4,5}$ yield

$$\begin{aligned} &\frac{A_0}{2} - 1 + \left[\frac{3-2\nu}{8(1-\nu)}A_1 - \frac{B_1 + 2\lambda^3 A_1}{2\lambda(1+\chi_2)} + 1 + \frac{u_0}{\delta}\right]\cos\theta \\ &\quad - \sum_{n=2}^{\infty}\left\{\left[\frac{\gamma_n}{n+1} - 2(1-\nu)(1+\chi_n)\right]\frac{A_n}{n-1} + 2(1-\nu)\frac{B_n}{\lambda}\right\}\frac{\cos n\theta}{\gamma_n} = 0, \end{aligned} \tag{3.7}$$

$$\begin{aligned} &\frac{4\lambda^3 A_1 + (1-\chi_1)B_1}{1+\chi_1}\cos\theta + \sum_{n=2}^{\infty}\left[16\lambda^3(1-\nu)nA_n + (2-\gamma_n)\,B_n\right]\frac{\cos n\theta}{\gamma_n} = \\ &\quad - 4\lambda^3\frac{R^2}{\delta}\kappa_0, \end{aligned} \tag{3.8}$$

for $0 \leq |\theta| \leq \alpha$, where:

$$\chi_n = \frac{K_{n+1}(1/\lambda)}{K_{n-1}(1/\lambda)}, \gamma_n = 1 + \chi_n + 8\lambda^2(1-\nu)(n-1)\,n. \tag{3.9}$$

To remove the unknown rigid body displacement u_0 and curvature κ_0, the operator

$$L[\phi] = \frac{\mathrm{d}\phi}{\mathrm{d}\theta} + \int_0^{\theta}\phi(s)\,\mathrm{d}s, \tag{3.10}$$

is applied on Eq. (3.7) and the difference between Eq. (3.8) evaluated at $\theta = 0$ and Eq. (3.8) is taken, thus obtaining

$$\frac{3-2\nu}{2(1-\nu)}\left(\frac{A_0}{2} - 1\right)\theta + \sum_{n=2}^{\infty}(f_n A_n + g_n B_n)\sin n\theta = 0, \tag{3.11}$$

$$\frac{4\lambda^3 A_1 + (1-\chi_1)B_1}{1+\chi_1}(1-\cos\theta) + \sum_{n=2}^{\infty}(h_n A_n + k_n B_n)(1-\cos n\theta) = 0 \tag{3.12}$$

for $0 \leq |\theta| \leq \alpha$, where:
for $0 \leq |\theta| \leq \alpha$, where:

$$\begin{aligned} f_n &= \frac{3-2\nu}{n}\left[\frac{1}{2(1-\nu)} - (n+1)\frac{1+\chi_n}{\gamma_n}\right], \\ g_n &= \frac{3-2\nu}{\lambda\,\gamma_n}\left(n - \frac{1}{n}\right), \\ h_n &= \frac{16\lambda^3(1-\nu)\,n}{\gamma_n}, \\ k_n &= \frac{2}{\gamma_n} - 1, \end{aligned} \tag{3.13}$$

for $n \geq 2$. Now, by considering that

$$\begin{aligned} \chi_n &= 4\lambda^2 n^2 + O(n), \\ \gamma_n &= 4\lambda^2(3-2\nu)\,n^2 + O(n), \end{aligned} \tag{3.14}$$

as $n \to \infty$, it follows that

$$\begin{aligned} f_n &= -1 + O\left(n^{-1}\right),\\ g_n &= \tfrac{1}{4\lambda^3 n} + O\left(n^{-2}\right),\\ h_n &= \tfrac{4\lambda(1-\nu)}{(3-2\nu)n} + O\left(n^{-2}\right),\\ k_n &= -1 + O\left(n^{-2}\right). \end{aligned} \tag{3.15}$$

Then, Eqs. (3.11) and (3.12) can be rewritten in the following form:

$$\begin{aligned} \sum_{n=1}^{\infty} A_n \sin n\theta &= \tfrac{3-2\nu}{2(1-\nu)}\left(\tfrac{A_0}{2}-1\right)\theta + A_1 \sin\theta\\ &+ \sum_{n=2}^{\infty}\left[\left(1+f_n\right)A_n + g_n B_n\right]\sin n\theta, \end{aligned} \tag{3.16}$$

$$\begin{aligned} \sum_{n=1}^{\infty} B_n(1-\cos n\theta) &= \frac{4\lambda^3 A_1 + 2B_1}{1+\chi_1}(1-\cos\theta)\\ &+ \sum_{n=2}^{\infty}\left[h_n A_n + (1+k_n)\,B_n\right](1-\cos n\theta), \end{aligned} \tag{3.17}$$

for $0 \le |\theta| \le \alpha$, where the series are convergent, according to the asymptotic behavior for $n \to \infty$ illustrated in Eqs. (3.15). Note that the contributions of the pin displacement u_0 and total curvature κ_0 do not appear in Eqs. (3.16)-(3.17), so that the unknown coefficients A_0, A_n, and B_n, for $n = 1, 2,\ldots$, do not depend on the values of u_0 and κ_0, which can instead be determined *a posteriori* from Eqs. (3.7) and (3.8) for $\theta = 0$, after the coefficients A_0, A_n, and B_n, for $n = 1, 2,\ldots$, have been obtained.

4. Governing equations in algebraic form

The coupled dual-series relations given in Eqs. (3.4), (3.30), and (3.31) are recast into an equivalent algebraic form for the unknown coefficients by extending the classical approach introduced by Sneddon (1966). This strategy, subsequently employed by Noble and Hussain (1969), Block and Keer, 2007 and more recently by Radi and Strozzi (2023), Radi (2026), and Radi and Güler (2026), is adapted here to the curvature-compatible formulation. The transformation relies on the introduction of two auxiliary stress functions, φ and ψ, through which the series relations are expressed in integral form

$$\frac{A_0}{2} + \sum_{n=1}^{\infty} A_n \cos n\theta = H(\alpha-\theta)\cos\frac{\theta}{2}\int_{\theta}^{\alpha}\frac{\varphi(s)\,\mathrm{d}s}{\sqrt{\cos\theta-\cos s}}, \tag{4.1}$$

$$\sum_{n=1}^{\infty} B_n \sin n\theta = H(\alpha-\theta)\sin\frac{\theta}{2}\int_{\theta}^{\alpha}\frac{\psi(s)\,\mathrm{d}s}{\sqrt{\cos\theta-\cos s}}, \tag{4.2}$$

for $0 \le \theta \le \pi$, where H denotes the Heaviside unit step function. Then, the coefficients A_0, A_n, and B_n, for $n = 1, 2,\ldots$ in the Fourier series (4.1) and (4.2) are

$$A_0 = \sqrt{2}\int_0^{\alpha}\varphi(s)\,\mathrm{d}s, \tag{4.3}$$

$$\begin{aligned} A_n &= \frac{1}{\sqrt{2}}\int_0^{\alpha}\left[P_{n-1}(\cos s) + P_n(\cos s)\right]\varphi(s)\,\mathrm{d}s,\\ B_n &= \frac{1}{\sqrt{2}}\int_0^{\alpha}\left[P_{n-1}(\cos s) - P_n(\cos s)\right]\psi(s)\,\mathrm{d}s, \end{aligned} \tag{4.4}$$

where P_n is the Legendre polynomial of order n, and the Mehler's integral for the Legendre polynomial (Sneddon, 1966, Eq. 2.6.20) has been used:

$$\int_0^{s}\frac{\cos(n+1/2)\theta}{\sqrt{\cos\theta-\cos s}}\mathrm{d}\theta = \frac{\pi}{\sqrt{2}}P_n(\cos s), \quad (n = 0, 1, 2, \ldots) \tag{4.5}$$

Now, using Eq. (4.4) and the following results (Srivastav (1963a) Eqs. (3.8), (4.7) and (4.8))

$$\frac{1}{\sqrt{2}}\sum_{n=1}^{\infty}\left[P_n(\cos s) + P_{n-1}(\cos s)\right]\sin n\theta = \frac{H(\theta-s)\cos(\theta/2)}{\sqrt{\cos s-\cos\theta}}, \tag{4.6}$$

$$\frac{1}{\sqrt{2}}\sum_{n=1}^{\infty}\left[P_{n-1}(\cos s) - P_n(\cos s)\right](1-\cos n\theta) = \frac{H(\theta-s)\sin(\theta/2)}{\sqrt{\cos s-\cos\theta}}, \tag{4.7}$$

from Eqs. (3.16) and (3.17), it follows

$$\begin{aligned} \int_0^{\theta}\frac{\varphi(s)\,\mathrm{d}s}{\sqrt{\cos s-\cos\theta}} &= \frac{1}{\cos(\theta/2)}\left\{\frac{3-2\nu}{2(1-\nu)}\left(\frac{A_0}{2}-1\right)\theta + A_1\sin\theta\right.\\ &\left.+\sum_{n=2}^{\infty}\left[(1+f_n)A_n + g_n B_n\right]\sin n\theta\right\}, \end{aligned} \tag{4.8}$$

$$\begin{aligned} \int_0^{\theta}\frac{\psi(s)\,\mathrm{d}s}{\sqrt{\cos s-\cos\theta}} &= \frac{1}{\sin(\theta/2)}\left\{\frac{4\lambda^3 A_1 + 2B_1}{1+\chi_1}(1-\cos\theta)\right.\\ &\left.+\sum_{n=2}^{\infty}\left[h_n A_n + (1+k_n)\,B_n\right](1-\cos n\theta)\right\} \end{aligned} \tag{4.9}$$

for $0 \le \theta \le \alpha$. Eqs. (4.8) and (4.9) are two integral equations of the Abel type that can be inverted following the approach of Srivastav (1963b) (see Appendix B) to obtain the auxiliary stress functions φ and ψ in terms of the unknown coefficients A_0, A_n, and B_n, for $n = 1, 2,\ldots$, namely

$$\begin{aligned} \varphi(s) = \frac{2}{\pi}\frac{\mathrm{d}}{\mathrm{d}s}\int_0^{s}\frac{\sin(\theta/2)}{\sqrt{\cos\theta-\cos s}}&\left\{\frac{3-2\nu}{2(1-\nu)}\left(\frac{A_0}{2}-1\right)\theta + A_1\sin\theta\right.\\ &\left.+\sum_{n=2}^{\infty}\left[(1+f_n)A_n + g_n B_n\right]\sin n\theta\right\}\mathrm{d}\theta, \end{aligned} \tag{4.10}$$

$$\begin{aligned} \psi(s) = \frac{2}{\pi}\frac{\mathrm{d}}{\mathrm{d}s}\int_0^{s}\frac{\cos(\theta/2)}{\sqrt{\cos\theta-\cos s}}&\left\{\frac{4\lambda^3 A_1 + 2B_1}{1+\chi_1}(1-\cos\theta)\right.\\ &\left.+\sum_{n=2}^{\infty}\left[h_n A_n + (1+k_n)B_n\right](1-\cos n\theta)\right\}\mathrm{d}\theta, \end{aligned} \tag{4.11}$$

The integrals in Eqs (4.10) and (4.11) can be calculated in closed form using the following identity provided in the Appendix in Radi and Strozzi (2023)

$$\frac{\mathrm{d}}{\mathrm{d}s}\int_0^{s}\frac{\theta\,\sin(\theta/2)}{\sqrt{\cos\theta-\cos s}}\,\mathrm{d}\theta = -\sqrt{2}\,\pi\,\frac{\mathrm{d}}{\mathrm{d}s}\ln\left(\cos\frac{s}{2}\right) = \frac{\pi}{\sqrt{2}}\tan\frac{s}{2}, \tag{4.12}$$

and the following results obtained by using Eq. (4.5)

$$\begin{aligned} \frac{\mathrm{d}}{\mathrm{d}s}\int_0^{s}\frac{\sin(\theta/2)\,\sin n\theta}{\sqrt{\cos\theta-\cos s}}\,\mathrm{d}\theta &= \frac{\pi}{2\sqrt{2}}\frac{\mathrm{d}}{\mathrm{d}s}\left[P_{n-1}(\cos s) - P_n(\cos s)\right]\\ &= \frac{\pi\,n}{2\sqrt{2}}\left[P_{n-1}(\cos s) + P_n(\cos s)\right]\tan\frac{s}{2}, \end{aligned} \tag{4.13}$$

$$\begin{aligned} \frac{\mathrm{d}}{\mathrm{d}s}\int_0^{s}\frac{\cos(\theta/2)\,(1-\cos n\theta)}{\sqrt{\cos\theta-\cos s}}\,\mathrm{d}\theta &= \frac{\pi}{2\sqrt{2}}\frac{\mathrm{d}}{\mathrm{d}s}\left[2 - P_n(\cos s) - P_{n-1}(\cos s)\right]\\ &= \frac{\pi\,n}{2\sqrt{2}}\left[P_{n-1}(\cos s) - P_n(\cos s)\right]\cot\frac{s}{2}, \end{aligned} \tag{4.14}$$

for $n = 1, 2, 3,\ldots$, thus obtaining

$$\begin{aligned} \varphi(s) = \tfrac{1}{\sqrt{2}}&\left\{\tfrac{3-2\nu}{1-\nu}\left(\tfrac{A_0}{2}-1\right) + A_1(1+\cos s)\right.\\ &\left.+\sum_{n=2}^{\infty} n\left[\left(1+f_n\right)A_n + g_n B_n\right]\left[P_n(\cos s) + P_{n-1}(\cos s)\right]\right\}\tan\tfrac{s}{2}, \end{aligned} \tag{4.15}$$

$$\psi(s)=\frac{1}{\sqrt{2}}\left\{\frac{4\lambda^3A_1+2B_1}{1+\chi_1}\sin s+\sum_{n=2}^{\infty}n\left[h_nA_n+(1+k_n)B_n\right]\left[P_{n-1}(\cos s)-P_n(c\right.\right.$$

Then, the introduction of Eqs. (4.15) and (4.16) in Eqs. (4.3) and (4.4) yields the following linear system of infinite algebraic equations for the coefficients A_0, A_n, and B_n, for $n = 1, 2,\ldots$:

$$A_0=\frac{3-2\nu}{1-\nu}(2-A_0)\ln\cos\frac{\alpha}{2}+A_1(1-\cos\alpha)+\sum_{j=2}^{\infty}j\left[(1+f_j)A_j+g_jB_j\right]J_j, \quad (4.17)$$

$$A_n=\frac{1}{2}\left\{\frac{3-2\nu}{1-\nu}\left(\frac{A_0}{2}-1\right)J_n+A_1K_{n1}+\sum_{j=2}^{\infty}jK_{nj}\left[(1+f_j)A_j+g_jB_j\right]\right\}, \quad (4.18)$$

$$B_n=\frac{2\lambda^3A_1+B_1}{1+\chi_1}L_n+\frac{1}{2}\sum_{j=2}^{\infty}jH_{nj}[h_jA_j+(1+k_j)B_j] \quad (4.19)$$

where (Radi and Strozzi, 2023):

$$J_n=\int_0^{\alpha}[P_n(\cos s)+P_{n-1}(\cos s)]\tan\frac{s}{2}\,\mathrm{d}s=\frac{P_{n-1}(\cos\alpha)-P_n(\cos\alpha)}{n},$$

$$K_{nj}=\int_0^{\alpha}\left[P_n(\cos s)+P_{n-1}(\cos s)\right]\left[P_j(\cos s)+P_{j-1}(\cos s)\right]\tan\tfrac{s}{2}\mathrm{d}s$$
$$=\frac{(1+\cos\alpha)\sin^2\alpha}{2(n^2-j^2)}\left[(n+1)P_{j-1}^{(0,1)}(\cos\alpha)P_{n-2}^{(1,2)}(\cos\alpha)-(j+1)P_{n-1}^{(0,1)}(\cos\alpha)P_{j-2}^{(1,2}\right.$$

$$L_n=\int_0^{\alpha}\left[P_{n-1}(\cos s)-P_n(\cos s)\right]\sin s\,\mathrm{d}s$$
$$=\begin{cases}\left(\dfrac{\cos\alpha}{n+1}-\dfrac{1}{n-1}\right)P_n(\cos\alpha)+\left(\dfrac{\cos\alpha}{n-1}-\dfrac{1}{n+1}\right)P_{n-1}(\cos\alpha), & \text{for n}\geqslant 2\\ 2\sin^4(\alpha/2), & \text{for } n=1\end{cases}$$

$$H_{nj}=\int_0^{\alpha}\left[P_{n-1}(\cos s)-P_n(\cos s)\right]\left[P_{j-1}(\cos s)-P_j(\cos s)\right]\cot\tfrac{s}{2}\mathrm{d}s=$$
$$=\frac{(1-\cos\alpha)\sin^2\alpha}{2(n^2-j^2)}\left[(n+1)P_{j-1}^{(1,0)}(\cos\alpha)P_{n-2}^{(2,1)}(\cos\alpha)-(j+1)P_{n-1}^{(1,0)}(\cos\alpha)P_{j-2}^{(2,1}\right.$$

being $P_n^{(a,b)}(t)$ the Jacobi polynomial of order n, and $P_n^{(0,0)}(t) = P_n(t)$. Note that $J_n \to 0$ and $L_n \to 0$ as $n \to \infty$. The details of the derivation of Eq. (4.20) can be found in Appendix A. However, the coefficients K_{nn} and H_{nn} must be calculated as limits for $j \to n$, namely

$$K_{nn}=\frac{(1+\cos\alpha)\sin^2\alpha}{4n}\left\{P_{n-1}^{(0,1)}(\cos\alpha)P_{n-2}^{(1,2)}(\cos\alpha)+(n+1)\times\right.$$
$$\left.\left[P_{n-1}^{(0,1)}(\cos\alpha)\tfrac{\mathrm{d}}{\mathrm{d}n}P_{n-2}^{(1,2)}(\cos\alpha)-P_{n-2}^{(1,2)}(\cos\alpha)\tfrac{\mathrm{d}}{\mathrm{d}n}P_{n-1}^{(0,1)}(\cos\alpha)\right]\right\}. \quad (4.21)$$

$$H_{nn}=\frac{(1-\cos\alpha)\sin^2\alpha}{4n}\left\{P_{n-1}^{(1,0)}(\cos\alpha)P_{n-2}^{(2,1)}(\cos\alpha)+(n+1)\times\right.$$
$$\left.\left[P_{n-1}^{(1,0)}(\cos\alpha)\tfrac{\mathrm{d}}{\mathrm{d}n}P_{n-2}^{(2,1)}(\cos\alpha)-P_{n-2}^{(2,1)}(\cos\alpha)\tfrac{\mathrm{d}}{\mathrm{d}n}P_{n-1}^{(1,0)}(\cos\alpha)\right]\right\}. \quad (4.22)$$

An approximate solution of Eqs. (4.17)–(4.19) is constructed by truncating the series expansion to a sufficiently large order N. The unknown coefficients A_0, A_n, and B_n, for $n = 1, 2,\ldots, N$, are determined from the resulting finite system, after which the parameters appearing in the field expressions (2.1) are evaluated using Eqs. (3.5) and (3.6) as

$$a_0=A_0/2, b_1=A_1/2, a_1=\frac{B_1+2\lambda^3A_1}{K_0(1/\lambda)+K_2(1/\lambda)} \quad (4.23)$$

$$a_n=\frac{8\lambda^3(1-\nu)nA_n+B_n}{\gamma_nK_{n-1}(1/\lambda)}, b_n=\frac{1}{2\gamma_n}\left(\frac{B_n}{\lambda}-\frac{1+\chi_n}{n-1}A_n\right), \quad (4.24)$$

for $n \geq 2$. The applied load P follows from integration of the contact pressure over the contact region along the loading direction.

$$P=-2R\int_0^{\alpha}\sigma_{rr}(1,\theta)\cos\theta\,\mathrm{d}\theta \quad (4.25)$$

By using Eq. $(3.3)_1$, (3.5), and (3.6), then Eq. (4.25) yields

$$P=-4\mu\delta\int_0^{\alpha}\left(\frac{A_0}{2}+\sum_{n=1}^{\infty}A_n\cos n\theta\right)\cos\theta\,\mathrm{d}\theta \quad (4.26)$$

The definite integral in Eq. (4.26) can be calculated analytically, thus providing

$$P=-4\mu\delta\left[\frac{A_0}{2}\sin\alpha+\frac{A_1}{2}\left(\alpha+\frac{\sin 2\alpha}{2}\right)\right.$$
$$\left.+\sum_{n=2}^{\infty}A_n\frac{n\cos\alpha\,\sin n\alpha-\sin\alpha\,\cos n\alpha}{n^2-1}\right] \quad (4.27)$$

Once the unknown coefficients A_0, A_n, and B_n, for $n = 1, 2,\ldots, N$, have been calculated, then using Eqs. (3.5), and (3.6), the rigid body motion of the pin follows from Eq. $(3.3)_2$ for $\theta = 0$ as

$$\frac{u_0}{\delta}=-\frac{A_0}{2}+\left[\frac{\lambda^2}{1+\chi_1}-\frac{3-2\nu}{8(1-\nu)}\right]A_1+\frac{B_1}{2\lambda(1+\chi_1)}$$
$$+\sum_{n=2}^{\infty}\left\{2\frac{1-\nu}{\lambda\,\gamma_n}B_n+\left[\frac{1}{n+1}-2(1-\nu)\frac{1+\chi_n}{\gamma_n}\right]\frac{A_n}{n-1}\right\}, \quad (4.28)$$

and the curvature κ_0 introduced in the contact condition $(2.3)_5$ follows from Eq. (3.8) for $\theta = 0$ as

$$\frac{R^2}{\delta}\kappa_0=-\frac{4\lambda^3A_1+(1-\chi_1)B_1}{4\lambda^3(1+\chi_1)}-\sum_{n=2}^{\infty}\left[\frac{4(1-\nu)}{\gamma_n}nA_n+\left(\frac{2}{\gamma_n}-1\right)\frac{B_n}{4\lambda^3}\right]. \quad (4.29)$$

The same value for κ_0 is obtained if Eq. (3.8) is evaluated at $\theta \neq 0$, for $0 < \theta < \alpha$, if Eq. (3.12) holds true.

5. Results

The numerical evaluation is carried out under plane-strain conditions for a representative Poisson's ratio $\nu = 0.3$. For prescribed values of the contact half-angle, the stress, couple-stress, and displacement fields are computed using the formulation described in Sect. 4, and the corresponding pin load is obtained through integration of the contact pressure along the active contact arc. The algebraic system of infinite equations (4–17)-(4.19) is truncated at $N = 60$, which ensures stable and accurate results for all parameter combinations considered. To suppress Gibbs-type oscillations in the graphical representation of the trigonometric expansions, Lanczos sigma factors (Lanczos, 1956) are applied to the stress and displacement series.

The subsequent analysis focuses on the influence of transmitted couple tractions on both the extent of the contact region and the spatial distribution of contact pressure, stress, couple-stress, displacement, and microrotation near the hole boundary. For a comprehensive visualization of the mechanical response, the distributions of the normalized von Mises equivalent stress σ_{eq} are also presented (de Borst, 1993; Zisis et al., 2018), where

$$\sigma_{eq}=\sqrt{3\left[\frac{1+\nu^2}{2}\left(\sigma_{rr}^2+\sigma_{\theta\theta}^2\right)+\nu^2\sigma_{rr}\sigma_{\theta\theta}+\frac{\left(\sigma_{r\theta}+\sigma_{\theta r}\right)^2}{4}+\frac{m_r^2+m_\theta^2}{2\ell}\right]} \quad (5.1)$$

Fig. 2a and b display the normalized pin load $P/\mu\delta$ as functions of the contact half-angle α/π and the normalized pin displacement u_0/δ, respectively, for various characteristic length ratio λ. As expected, either an increase in the applied load P or a reduction in the clearance δ results in an expansion of the contact zone. The plots in Fig. 2 also

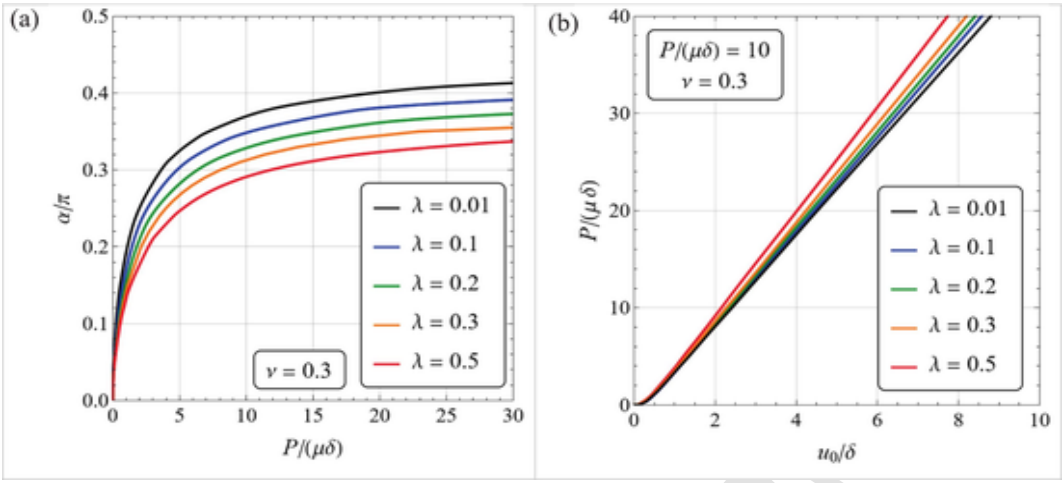

Fig. 2. Variation of the normalized pin load P with respect to the contact half-angle α (a) and the corresponding rigid pin displacement u_0 (b), for different characteristic length ratios $\lambda = \ell/R$.

demonstrate that, under a prescribed load P, both the contact angle α and the pin displacement u_0 reduce appreciably with increasing characteristic length ratio. This reduction directly reveals the enhanced resistance to curvature gradients induced by couple-stress elasticity and underlines the significant size-dependent behavior intrinsic to the theory.

Similarly, the average and peak values of the contact pressure rise as λ increases. This tendency is evident from Fig. 3a, where the normalized distribution of the contact pressure along the boundary of the hole is illustrated for different characteristic length ratios, under the same pin load $P = 10\ \mu\delta$. The contact pressure attains its maximum at the center of the contact region and it decreases to zero at the extremities. Its magnitude increases with the characteristic length ratio, as previously observed for the couple-traction-free contact condition by Radi and Güler (2026). The same qualitative trend is obtained when curvature is prescribed and non-zero couple tractions develop along the contact arc. However, in this case, the maximum contact pressure is slightly higher than in the couple-traction-free configuration, and the difference becomes more pronounced as λ increases. In the limit as $\ell \to 0$, the solution asymptotically approaches the classical Hertzian-type elliptical pressure distribution, consistent with previous observations reported in Radi and Güler (2026) neglecting couple tractions.

The present formulation does not guarantee a priori that the resulting contact pressure remains compressive over the entire contact zone. However, this condition is verified a posteriori from the obtained solution. The results reported in Fig. 3a show that, for the parameter ranges considered, the pressure distributions are compressive within the contact region and vanish smoothly at the contact edges, thereby confirming the consistency of the adopted formulation for those cases.

The distributions of hoop stress, $\sigma_{\theta\theta}$, shear stress $\sigma_{\theta r}$, von Mises equivalent stress σ_{eq}, and couple-stresses m_r and m_θ along the hole rim are presented in Fig. 3b-f. From these plots, it can be observed that magnitude of all stress and couple-stress components within the contact region increase with the characteristic length ratio λ. However, the qualitative response differs notably from that observed under the couple-traction-free contact conditions in Radi and Güler (2026). In particular, the couple tractions m_r, plotted in Fig. 3f, now display significant values along the contact arc as λ increases, whereas the hoop stress $\sigma_{\theta\theta}$ and the tangential couple-stress m_θ, plotted in Fig. 3b and 3e respectively, remarkably decrease with respect to their distribution in the couple-traction-free case and tend to assume more uniform distributions within the contact region. Since the hoop stress is the primary driver of radial crack initiation and propagation, its magnitude is directly relevant to structural integrity assessments. Consistent with the contact condition of uniform tangential curvature assumed in Eq. $(2.3)_5$, the tangential couple-stress m_θ exhibits a uniform distribution along the contact zone, whose magnitude increases with the characteristic length ratio, being $m_\theta = 2\mu\ell^2\kappa_0$.

Fig. 4a and b depict the variations of hoop stress along the radial lines $\theta = 0$ and $\theta = \alpha$, respectively. The effects of the microstructural characteristic length are more pronounced in the immediate vicinity of the hole surface. Compared with the couple-traction-free contact condition, the hoop stress along the radial direction $\theta = 0$ decreases remarkably as λ increases, whereas a slight increase is observed along the radial direction $\theta = \alpha$. These findings support the conclusion that couple-stress elasticity primarily modifies stress gradients in regions characterized by high curvature or intense deformation. In this case as well, the stress field becomes essentially independent of λ beyond a radial distance of approximately $3R$, denoting that the microstructural effects remain confined to the neighbourhood of the contact interface.

As observed in Radi and Güler (2026) for the couple-traction-free contact condition, the radial and tangential displacement components, u_r and u_θ, shown in Fig. 5a and 5b, decrease in magnitude and display a more uniform distribution along the hole rim as λ increases. This behavior indicates that incorporating microstructural effects leads to a stiffer overall material response.

The normalized distributions of rotation ω_z along the hole rim are illustrated in Fig. 5c for several microstructural ratios λ. In accordance with the assumption of a uniform distribution of tangential curvature in Eq. $(2.3)_5$, the microrotation varies linearly with the angular coordinate θ within the contact region, reaching its maximum at the edge of the contact arc ($\theta = \alpha$). Its magnitude systematically decreases as the characteristic length ratio increases, a trend attributed to the higher rotational stiffness predicted by the constrained theory of couple-stress elasticity (Weitsman, 1965), thereby confirming the stiffening effect introduced by the microstructure.

The corresponding variation of the normalized tangential curvature κ_0 along the contact arc with the characteristic length ratio λ, depicted in Fig. 5d, shows that the curvature decreases as $\lambda^{-1/2}$ as λ increases thus confirming that the curvature is significantly smoothed out by the material resistance to bending. The intrinsic length $\ell = \lambda R$ controls the weight of the curvature contribution in the strain energy, which scales with ℓ^2. As $\lambda \to 0$, this contribution vanishes, and the governing equations reduce to those of classical elasticity, in which curvature is not an independent energetic variable. In this limit, the higher-order stresses associated with the curvature tensor disappear, and the boundary con-

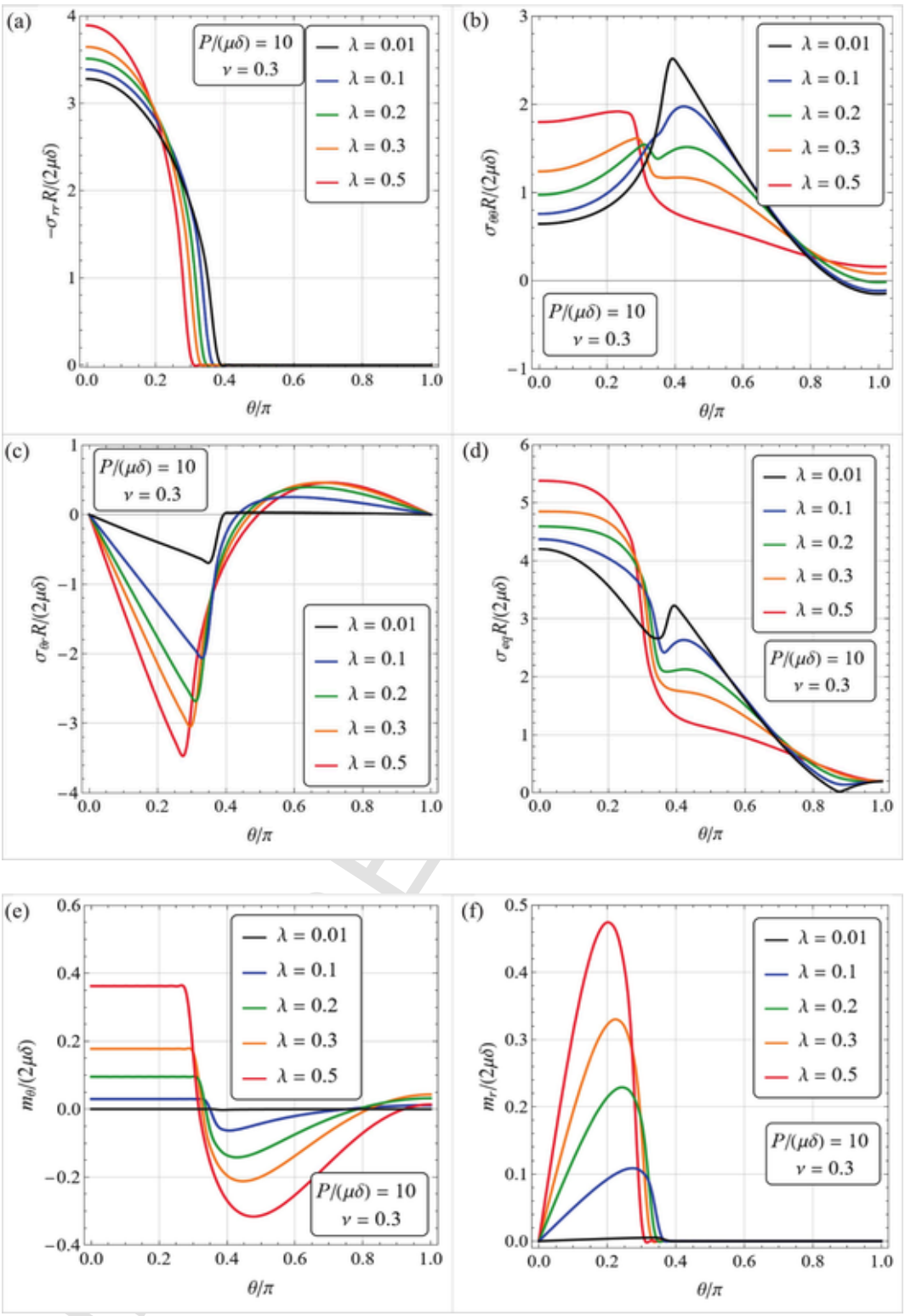

Fig. 3. Angular variation of the contact pressure (a), hoop stress (b), shear stress (c), and circumferential couple-stress (d) along the hole rim ($r = R$), illustrating the effect of curvature-induced couple tractions for representative characteristic length ratios under a constant pin load $P = 10\ \mu\delta$.

dition on curvature loses its mechanical significance. More precisely, the curvature field becomes asymptotically decoupled from the displacement and stress fields, so that the parameter κ_0 no longer influences the classical elastic solution. Although Fig. 5d shows that κ_0 tends to a finite non-zero value as $\lambda \to 0$, this does not imply a residual mechanical effect. The reason is that the energetic and constitutive coupling between curvature and stress vanishes with λ, so that κ_0 becomes mechanically inactive and does not affect the equilibrium solution. In this sense, the curvature condition becomes asymptotically redundant, and the solution smoothly reduces to the classical pin-hole contact

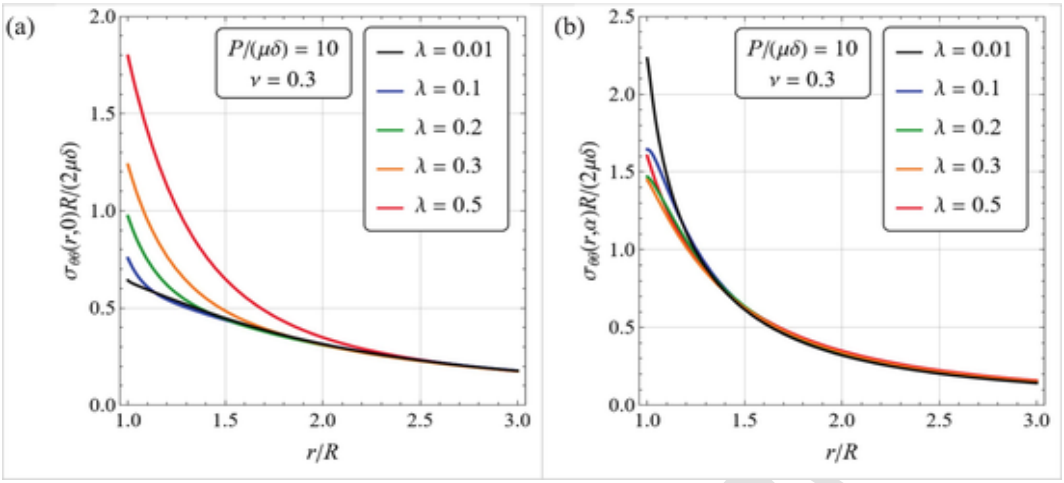

Fig. 4. Distributions of normalized hoop stress along the radial directions $\theta = 0$ (a), and $\theta = \alpha$ (b) as functions of the radial coordinate r, for a fixed pin load $P = 10$ μδ.

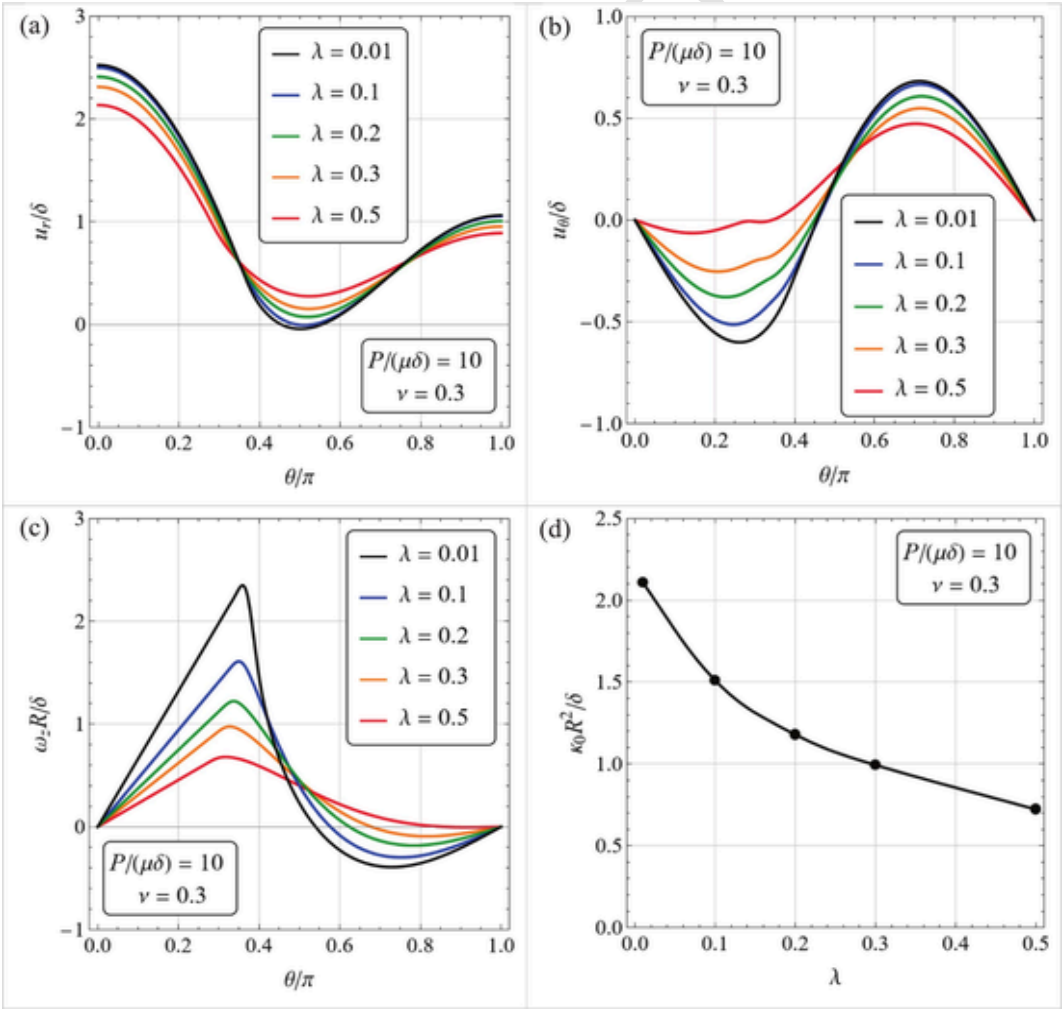

Fig. 5. Angular variation of radial displacement (a), tangential displacement (b), and microrotation (c) along the hole boundary ($r = R$) demonstrating the kinematic response under curvature-compatible contact conditions. The corresponding evolution of the normalized tangential curvature κ_0 with the characteristic length ratio $\lambda = \ell/R$ is also shown, for a fixed applied load $P = 10$ μδ.

problem. Physically, the persistence of a finite κ_0 reflects the fact that, in the absence of couple-stress effects, rotation gradients are not penalized energetically and therefore do not contribute to the mechanical response. As λ increases, curvature becomes energetically relevant, and κ_0 decreases as a consequence of the strain energy minimization.

The analytical profiles of the normalized von Mises equivalent stress, σ_{eq}, in the region surrounding the hole are presented in Fig. 6 for three representative values of the characteristic length ratio λ, all corresponding to the same pin load, $P = 10\ \mu\delta$. When λ is small, the peak equivalent stress is located at the midpoint of the contact arc ($\theta = 0$), consistent with the classical contact solution. As λ increases, a distinct transition occurs: the maximum equivalent stress shifts toward the boundaries of the contact zone and appears slightly below the hole surface. This displacement of the stress peak underscores the crucial influence of the material length scale, which alters the stress distribution by transferring the concentration from the central loading area to inner regions near the contact edges, where deformation gradients are more pronounced.

5.1. Comparison with results for vanishing couple tractions

A comparison between the results obtained in the present formulation and those reported by Radi and Güler (2026), which considered the same pin–hole configuration under micro-free (vanishing couple-traction) contact conditions, for identical values of P, λ, and ν, shows that the introduction of curvature compatibility and associated couple tractions leads to the following specific effects, beyond those already associated with increasing λ:

- a slight increase in the maximum contact pressure and shear stress is observed along the contact region when couple tractions are included. This reflects the additional kinematic constraint imposed at the interface, which reduces local compliance.
- a more pronounced redistribution of the hoop stress occurs, characterized by a reduction in its peak value at the contact edges and a shift of the maximum toward the center of the contact arc. While a similar trend was observed in Radi and Güler (2026), the present formulation produces a significantly stronger reduction of the maximum hoop stress for larger values of the characteristic length;
- a substantial modification of the couple-stress field: in the present case, radial couple tractions develop along the contact arc, and the tangential couple traction becomes nearly uniform and significantly smaller than the peak values observed under micro-free conditions.

At the same time, it is observed that the overall distribution of displacements and equivalent von Mises stress exhibits similar qualitative trends in both formulations, indicating that the curvature-compatible condition primarily affects the redistribution and localization of stresses rather than their global structure, producing a smoother and more uniform stress distribution along the contact arc. These comparisons demonstrate that the trends associated with increasing λ (such as stiffening and reduction of contact angle) are primarily governed by couple-stress elasticity itself, whereas the curvature-compatible contact condition introduces additional effects, mainly related to stress and couple-stress redistribution.

5.2. Convergence of the series expansions

To investigate the convergence of the series in Eqs. (4.17)–(4.19) as the number of retained terms N increases, the coefficient ratios A_n/A_0 (for $0 \le n \le N$) and B_n/B_1 (for $1 \le n \le N$) are plotted in Fig. 7. The results shown correspond to a truncated series expansion with $N = 60$ terms, for various characteristic length ratios λ, under the same applied pin load $P = 10\ \mu\delta$. From these plots, it can be observed that the higher-order coefficients A_n and B_n with $n > 60$ are practically negligible with respect to the leading order terms A_0 and B_1 for all the considered values of the characteristic length ratio .

As reported in Radi and Güler (2026), a large number of terms is required only for very small contact arc, whereas convergence becomes more rapid for larger contact regions for every set of material parame-

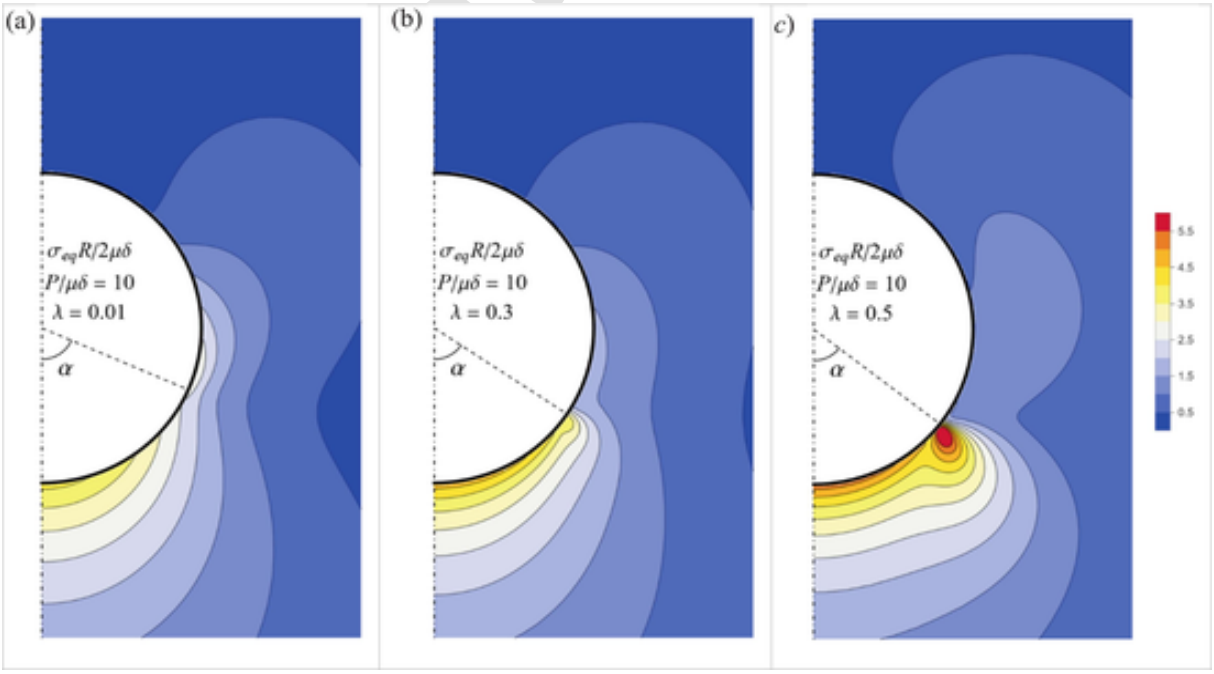

Fig. 6. Contour plots of the normalized von Mises equivalent stress, $\sigma_{eq}\,R/(2\mu\delta)$, in the vicinity of the hole under the curvature-compatible contact formulation. Results are shown for characteristic length $\lambda = 0.01$ (a), $\lambda = 0.3$ (b), and $\lambda = 0.5$ (c) at a fixed applied load $P/(\mu\delta) = 10$.

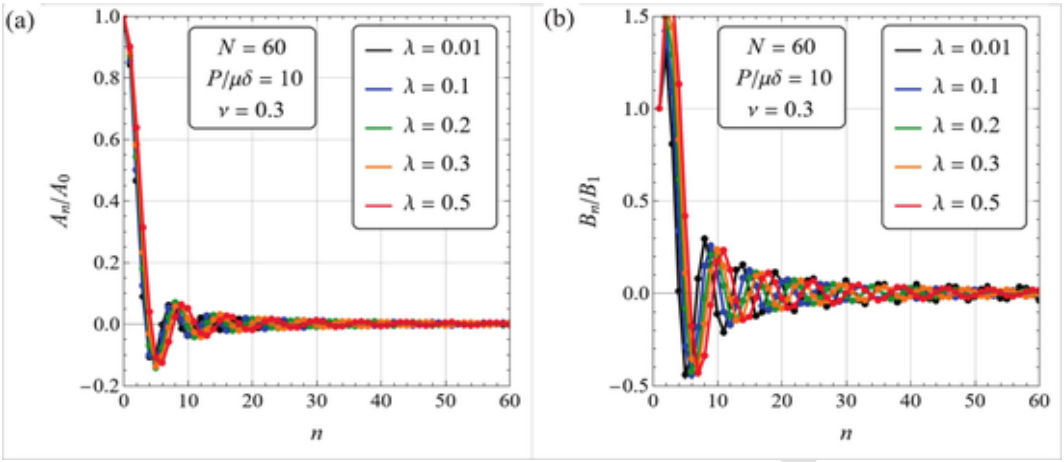

Fig. 7. Variations of the coefficient ratios A_n/A_0 (a), and B_n/B_1 (b), associated with the truncated system with $N = 60$, shown for representative characteristic length ratios under constant applied pin load $P = 10\ \mu\delta$.

ters. Therefore, for a sufficiently high pin load, as that considered in the results here presented, including 60 terms in the series expansions provides a consistently high degree of accuracy in the computed solution.

6. Conclusions

A closed-form analytical treatment is proposed for the frictionless contact problem of a rigid pin with clearance inserted into a hole in a couple-stress elastic plane with microstructure, under plane strain conditions, allowing for the transmission of couple tractions along the contact interface. This approach extends a previous work in which the contact region was assumed to be couple-traction-free. In the present formulation, the latter condition is replaced by the assumption of a uniform tangential curvature within the contact region.

The mechanical fields—namely stresses, couple-stresses, displacements, and rotations—were represented through Fourier-type trigonometric expansions, then reducing the frictionless contact problem into a coupled system of dual trigonometric series. A new approach has been proposed for recasting this system as an infinite set of linear algebraic equations, which can be easily solved after appropriate truncation. The developed procedure provides a systematic and accurate framework for analyzing contact problems in higher-order continua, which can be reduced to a pair of coupled dual trigonometric series equations.

When curvature is prescribed along the contact arc, leading to nonzero couple tractions at the interface, the mechanical response differs qualitatively from the couple-traction-free configuration. Indeed, the stress and couple-stress fields near the hole boundary are significantly redistributed. In particular, the hoop stress and tangential couple-stress decrease significantly compared to the couple-traction-free case, and their distribution become more uniform within the contact region. These findings underline the sensitivity of higher-order contact problems to the choice of boundary conditions and highlight the physical relevance of curvature compatibility at the microscale.

Overall, the analysis demonstrates that the presence of an intrinsic material length scale, characteristic of couple-stress elasticity, introduces pronounced size-dependent effects in cylindrical joints and pin-hole assemblies. Such effects are localized in the vicinity of the contact interface but may substantially alter stress concentrations and structural response when the characteristic length becomes comparable to the contact dimensions. The proposed formulation therefore provides a useful theoretical framework for the analysis and design of micro-scale mechanical joints, architected materials, and other systems in which classical elasticity is inadequate to describe the observed behavior. The present study is particularly relevant for the modeling and design of cylindrical joints operating at small length scales, where microstructural effects cannot be neglected. Practical applications include precision micro-mechanical assemblies, such as micro-pins and bushings in MEMS devices, biomedical implants with press-fit or clearance-based fixation, and miniaturized mechanical couplings used in aerospace and high-performance instrumentation. In such systems, the characteristic dimensions of the joint may become comparable to the intrinsic material length scale, making curvature-induced couple tractions significant in determining contact pressure, stress localization, and overall stiffness. The proposed formulation is also pertinent to additively manufactured components and architected or gradient materials, where internal microstructure and geometric constraints strongly influence local rotation gradients at contact interfaces. By accounting for curvature compatibility and the associated transmission of couple tractions, the model provides a more realistic prediction of stress redistribution, potential crack initiation sites, and size-dependent stiffening effects in advanced cylindrical joints and pin-hole assemblies.

Uncited reference

.

CRediT authorship contribution statement

E. Radi: Writing – original draft, Visualization, Software, Methodology, Investigation, Formal analysis, Conceptualization. **M.A. Güler:** Writing – review & editing, Supervision, Investigation, Conceptualization.

Declaration of competing interest

The authors declare that they have no known competing financial interests or personal relationships that could have appeared to influence the work reported in this paper.

Acknowledgments

Support by the National Group of Mathematical Physics (GNFM-INdAM) is gratefully acknowledged.

Data availability

No data was used for the research described in the article.

Appendix A. . Integral involving Legendre and Jacobi polynomials

To calculate the definite integrals (4.20) we use the following relations provided in Szegö (1939) in Eq. (4.5.4):

$$\begin{aligned} P_n(t) + P_{n-1}(t) &= (1+t)\,P_{n-1}^{(0,1)}(t), \\ P_n(t) - P_{n-1}(t) &= (1-t)\,P_{n-1}^{(1,0)}(t), \end{aligned} \tag{A.1}$$

and the following results obtained by Derevyagin and Juricic (2020) in their Eq. (3.3):

$$\begin{aligned} \int_x^1 (1+t)P_{n-1}^{(0,1)}(t)P_{m-1}^{(0,1)}(t)\,\mathrm{d}t = \frac{(1+x)(1-x^2)}{2(n^2-m^2)}[&(n+1)P_{m-1}^{(0,1)}(x)P_{n-2}^{(1,2)}(x) \\ &-(m+1)P_{n-1}^{(0,1)}(x)P_{m-2}^{(1,2)}(x)] \end{aligned}$$

$$\begin{aligned} \int_x^1 (1-t)P_{n-1}^{(1,0)}(t)P_{m-1}^{(1,0)}(t)\,\mathrm{d}t = \frac{(1-x)(1-x^2)}{2(n^2-m^2)}[&(n+1)P_{m-1}^{(1,0)}(x)P_{n-2}^{(2,1)}(x) \\ &-(m+1)P_{n-1}^{(1,0)}(x)P_{m-2}^{(2,1)}(x)] \end{aligned} \tag{A.2}$$

Then

$$\begin{aligned} K_{nm} &= \int_0^\alpha \left[P_n(\cos s) + P_{n-1}(\cos s)\right]\,\left[P_m(\cos s) + P_{m-1}(\cos s)\right]\tan\tfrac{s}{2}\,\mathrm{d}s = \\ &= \int_{\cos\alpha}^1 \left[P_n(t) + P_{n-1}(t)\right]\,\left[P_m(t) + P_{m-1}(t)\right]\tfrac{\mathrm{d}t}{1+t} = \int_{\cos\alpha}^1 (1+t)\;P_{n-1}^{(0,1)}(t)\;P_{m-1}^{(0,1)}(t)\;\mathrm{d}t = \\ &= \tfrac{(1+\cos\alpha)\sin^2\alpha}{2(n^2-m^2)}\left[(n+1)\,P_{m-1}^{(0,1)}(\cos\alpha)\,P_{n-2}^{(1,2)}(\cos\alpha) - (m+1)\,P_{n-1}^{(0,1)}(\cos\alpha)\,P_{m-2}^{(1,2)}(\cos\alpha)\right], \end{aligned} \tag{A.3}$$

$$\begin{aligned} H_{nm} &= \int_0^\alpha \left[P_{n-1}(\cos s) - P_n(\cos s)\right]\,\left[P_{m-1}(\cos s) - P_m(\cos s)\right]\cot\tfrac{s}{2}\,\mathrm{d}s = \\ &= \int_{\cos\alpha}^1 \left[P_{n-1}(t) - P_n(t)\right]\,\left[P_{m-1}(t) - P_m(t)\right]\tfrac{\mathrm{d}t}{1-t} = \int_{\cos\alpha}^1 (1-t)\;P_{n-1}^{(1,0)}(t)\;P_{m-1}^{(1,0)}(t)\;\mathrm{d}t = \\ &= \tfrac{(1-\cos\alpha)\sin^2\alpha}{2(n^2-m^2)}\left[(n+1)\,P_{m-1}^{(0,1)}(\cos\alpha)\,P_{n-2}^{(1,2)}(\cos\alpha) - (m+1)\,P_{n-1}^{(0,1)}(\cos\alpha)\,P_{m-2}^{(1,2)}(\cos\alpha)\right], \end{aligned} \tag{A.4}$$

for $n \neq m$.

Appendix B. . Inversion of the integral equation of the Abel type

According to the approach of Srivastav (1963b), the integral equation of the Abel type

$$\int_0^\theta \frac{\varphi(s)\,\mathrm{d}s}{\sqrt{\cos s - \cos\theta}} = f(\theta) \tag{B.1}$$

with $0 \le \theta \le \pi$ and $f(0) = 0$, admits the following solution

$$\varphi(s) = \frac{1}{\pi}\frac{\mathrm{d}}{\mathrm{d}s}\int_0^s \frac{\sin\theta\, f(\theta)}{\sqrt{\cos\theta - \cos s}}\,\mathrm{d}\theta \tag{B.2}$$

Proof: by exchanging the order of integration we obtain:

$$\begin{aligned} &\int_0^s \frac{\sin\theta\, f(\theta)}{\sqrt{\cos\theta - \cos s}}\,\mathrm{d}\theta \\ &= \int_0^s \frac{\sin\theta\,\mathrm{d}\theta}{\sqrt{\cos\theta - \cos s}}\int_0^\theta \frac{\varphi(t)\;\mathrm{d}t}{\sqrt{\cos t - \cos\theta}} \\ &= \int_0^s \varphi(t)\;\mathrm{d}t\int_t^s \frac{\sin\theta\,\mathrm{d}\theta}{\sqrt{\cos t - \cos\theta}\sqrt{\cos\theta - \cos s}} \\ &= \pi\int_0^s \varphi(t)\;\mathrm{d}t. \end{aligned} \tag{B.3}$$

Then, by taking the derivative of Eq. (B.3) with respect to s, the solution (B.2) is recovered.

References

Ariman, T., 1967. On the stresses around a circular hole in micropolar elasticity. Acta Mech. 4 (3), 216–229.

Bhandakkar, T.K., 2023. Tabulation of Mindlin-Airy stress potentials and the corresponding stress and displacement in polar co-ordinates in couple-stress elasticity. Sādhanā 48, 24.

Bashash, S., Jalili, N., 2009. Robust adaptive control of coupled parallel piezo-flexural nano-positioning stages. IEEE/ASME Trans. Mechatron. 14 (1), 11–20.

Belfiore, N.P., Verotti, M., Crescenzi, R., Balucani, M., 2013. In: Design, Optimization and Construction of MEMS-Based Micro Grippers for Cell Manipulation. IEEE, pp. 105–110.

Block, J.M., Keer, L.M., 2007. Partial contact of an elastic coated cylinder pressed by a rigid flat surface. J. Tribol. 131, 024502.

Chong, A.C., Lam, D.C., 1999. Strain gradient plasticity effect in indentation hardness of polymers. J. Mater. Res. 14 (10), 4103–4110.

Das, R.N., 1969. The effect of couple-stresses on stress distribution in a thin plate due to the pressure of a rivet on one side of a circular hole. Cz. J. Phys. B 19 (1), 53–58.

de Borst, R., 1993. A generalisation of J2-flow theory for polar continua. Comput. Meth. Appl. Mech. Eng. 103 (3), 347–362.

Derevyagin, M., Juricic, N., 2020. An asymptotic formula for integrals of products of Jacobi polynomials. J. Stoch. Anal. 1 (4), 8.S.

Gao, Y.F., Larson, B.C., Lee, J.H., Nicola, L., Tischler, J.Z., Pharr, G.M., 2015. Lattice rotation patterns and strain gradient effects in face-centered-cubic single crystals under spherical indentation. J. Appl. Mech. 82 (6), 061007.

Gourgiotis, P.A., Zisis, T., Giannakopoulos, A.E., Georgiadis, H.G., 2019. The Hertz contact problem in couple-stress elasticity. Int. J. Solids Struct. 168, 228–237.

Hartranft, R.J., Shih, G.C., 1965. The effect of couple-stresses on the stress concentration of a circular inclusion. J. Appl. Mech. 32, 429–431.

Koiter, W., 1964. Couple-stresses in the theory of elasticity Parts I and II. Nederl. Akad. Wetensch. Proc. Ser. B. 67, 17–29.

Lanczos, C., 1956. Applied Analysis. Prentice Hall, Englewood Cliffs.

Lam, D.C., Yang, F., Chong, A.C.M., Wang, J., Tong, P., 2003. Experiments and theory in strain gradient elasticity. J. Mech. Phys. Solids 51 (8), 1477–1508.

Lee, J.H., Gao, Y., Bower, A.F., Xu, H., Pharr, G.M., 2018. Stiffness of frictional contact of dissimilar elastic solids. J. Mech. Phys. Solids 112, 318–333.

Mindlin, R.D., 1963. Influence of couple-stresses on stress concentrations. Exp. Mech. 3 (1), 1–7.

Nix, W.D., Gao, H., 1998. Indentation size effects in crystalline materials: a law for strain gradient plasticity. J. Mech. Phys. Solids 46 (3), 411–425.

Noble, B., Hussain, M.A., 1969. Exact solution of certain dual series for indentation and inclusion problems. Int. J. Eng. Sci. 7 (11), 1149–1161.

Peterson, B.T., Hardin, T.J., Pomeroy, A.W., Hopkins, J.B., Clites, T.R., 2023. Cross-axis flexural pivots in mechatronic applications: stress-based design for combined tension and bending. IEEE/ASME Trans. Mechatron. 29 (2), 913–923.

Persson, A. On the stress distribution of cylindrical elastic bodies in contact. PhD. Dissertation Chalmers University, Sweden, 1964.

Polit, S., Dong, J., 2011. Development of a high-bandwidth XY nanopositioning stage for high-rate micro-/nanomanufacturing. IEEE/ASME Trans. Mechatron. 16 (4), 724–733.

Radi, E., 2026. Stress shielding effects in pin-loaded hole contact with clearance using FGM. Int. J. Mech. Sci. https://doi.org/10.1016/j.ijmecsci.2025.111048.

Radi, E., Güler, M.A., 2026. Effects of microstructure in pin-loaded hole contact with clearance. Int. J. Eng. Sci. 221, 104454.

Radi, E., Strozzi, A., 2023. Advancing contact of a 2D elastic curved beam indented by a rigid pin with clearance. Int. J. Nonlin. Mech. 149, 104313.

Sneddon, I.N., 1966. Mixed boundary value problems in potential theory. John Wiley, New York.

Srivastav, R.P., 1963a. XVI.-dual series relations. III. dual relations involving trigonometric series. Proc. Royal Soc. Edinb. Sect. A: Math. 66 (3), 173–184.

Srivastav, R.P., 1963b. A note on certain integral equations of Abel-type. Proc. Edinb. Math. Soc. 13 (3), 271–272.

Szegö, G., 1939. Orthogonal Polynomials. Colloquium Publications, American Mathematical Society, Providence, Rhode Island, USA.

Verotti, M., Crescenzi, R., Balucani, M., Belfiore, N.P., 2015. MEMS-based conjugate surfaces flexure hinge. J. Mech. Design 137 (1), 012301.

Wang, D.H., Yang, Q., Dong, H.M., 2011. A monolithic compliant piezoelectric-driven microgripper: Design, modeling, and testing. IEEE/ASME Trans. Mechatron. 18 (1), 138–147.

Weitsman, Y., 1965. Couple-stress effects on stress concentration around a cylindrical inclusion in a field of uniaxial tension. ASME J. Appl. Mech. 32 (2), 424–428.

Xu, Q., 2012. Design and development of a flexure-based dual-stage nanopositioning system with minimum interference behavior. IEEE Trans. Autom. Sci. Eng. 9 (3), 554–563.

Zhang, X.M., Liu, A.Q., Lu, C., Tang, D.Y., 2007. A real pivot structure for MEMS tunable lasers. J. Microelectromechanical Syst. 16 (2), 269–278.

Zisis, Th., Gourgiotis, P.A., Baxevanakis, K.P., Georgiadis, H.G., 2014. Some basic contact problems in couple-stress elasticity. Int. J. Solids Struct. 51, 2084–2095.

Zisis, Th., Gourgiotis, P.A., Georgiadis, H.G., 2018. Contact mechanics in the framework of couple-stress elasticity. In: Altenbach, H. (Ed.), Generalized Models and Non-Classical Approaches in Complex Materials 2, Advanced Structured Materials, 90, Chapter 14. Springer, pp. 279–306.